International Journal of Hydrogen Energy 235 (2026) 155136

Contents lists available at ScienceDirect

International Journal of Hydrogen Energy

journal homepage: www.elsevier.com/locate/he

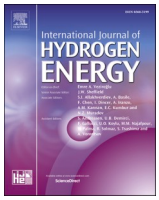

Quartz-enhanced photoacoustic detection of trace impurities in hydrogen: spectrophone design and CO sensing

Mariagrazia Olivieri [a], Andrea Zifarelli [a,*], Giansergio Menduni [a], Enrico Sallustio [a], Angelo Sampaolo [a,b], Vincenzo Spagnolo [a,b], Pietro Patimisco [a,b]

[a] PolySense Lab, Dipartimento Interateneo di Fisica M. Merlin, Università degli Studi di Bari Aldo Moro e Politecnico di Bari, Via G. Amendola 173, Bari, 70126, Italy
[b] PolySense Innovations srl, Via Amendola 173, Bari, 70126, Italy

ARTICLE INFO

Keywords:
Hydrogen impurities
Gas sensing
Photoacoustic spectroscopy

ABSTRACT

In this work, the use of Quartz-Enhanced Photoacoustic Spectroscopy (QEPAS) for the detection of CO impurities in hydrogen was demonstrated. Due to the high speed of sound in hydrogen, the geometry of the spectrophone was specifically selected to ensure efficient sound wave amplification. Therefore, a QEPAS spectrophone was designed by exploiting a custom quartz tuning fork operating at first overtone mode (~44,0 kHz) in combination with compact resonator tubes. The spectrophone was integrated into a QEPAS sensor for CO trace detection at 2193.36 cm^{-1} in a hydrogen matrix. The QEPAS sensor was calibrated using certified mixtures, returning a detection limit of 1.5 ppm for 10 s. Furthermore, pressure-dependent measurements enabled the determination of the effective V–T relaxation rate of CO in hydrogen, which was found to be 438 ± 80 s^{-1} $Torr^{-1}$.

1. Introduction

Today most of worldwide energy production is completely entrusted to fossil fuels, such as coal, oil and natural gas. Since the last half of the 20th century, it has been widely recognized within the scientific community that the extensive use of hydrocarbons is a major driver of global temperature rise and their economic costs significantly affect countries worldwide. In fact, the burning of fossil fuels releases huge amounts of greenhouse gases, mainly carbon dioxide, which significantly contribute to global warming. Therefore, the transition to green energy is essential, yet challenging to achieve. Hydrogen has emerged as a key enabler of cleaner energy systems [1–4]. Over the last twenty years, hydrogen has been increasingly promoted as a key energy carrier, accompanied by the development of the infrastructure required for its production, transport, and storage [5–8]. Hydrogen used as fuel offers an important advantage, as it burns without producing carbon dioxide. However, its primary limitation is that hydrogen is not freely available in nature but occurs only in combination with other elements, primarily oxygen (in water) and carbon (in hydrocarbons and other organic compounds). Nevertheless, hydrogen can be employed as energy carrier similarly to electricity, with its own distinct advantages and limitations. One of the main advantages is that hydrogen has the highest gravimetric energy density among all known fuels, as 1 kg of H_2 corresponds to ~3.2 kg of gasoline and ~2.1 kg of natural gas [8]. However, hydrogen used in fuel cells for energy production must meet purity standards established by international regulatory bodies [9–13]. The most important reference is ISO 14678, last updated in 2025, which defines the limits for trace contaminants in hydrogen fuel [14]. In Europe, the corresponding standard is EN 17124, approved in 2018, which adopts the same specification levels as the ISO directive.

The occurrence and composition of impurities in hydrogen samples strongly depends on the employed production method [15–17]. For example, carbon monoxide is commonly found in hydrogen samples produced by steam reforming, whereas contaminants such as oxygen are more prevalent when hydrogen is produced via chloro-alkali or water electrolysis, while ammonia is generated during the production or purification of hydrogen via ammonia cracking or as a by-product in reformers. Contaminants can lead to significant power losses and degradation of cell components, compromising both performance and lifetime. Different impurities affect different parts of the cell. Species such as carbon monoxide and sulfur compounds primarily affect the anode catalyst by adsorbing on active sites and inhibiting hydrogen oxidation, while contaminants like ammonia and halogenated compounds can degrade the polymer electrolyte membrane by reducing proton conductivity or inducing chemical damage. Other impurities, including water vapor, hydrocarbons, and particulates, interfere with

* Corresponding author.
E-mail address: andrea.zifarelli@uniba.it (A. Zifarelli).

https://doi.org/10.1016/j.ijhydene.2026.155136
Received 19 February 2026; Received in revised form 10 April 2026; Accepted 18 April 2026
Available online 22 April 2026

mass transport and water management by obstructing gas diffusion layers and flow channels. Table 1 reports the quality specification for fuel cell road vehicle applications according to ISO 14687 [14].

Various detection techniques can be used to identify and detect impurities in hydrogen [18–21]. These methods can be broadly divided into analytical techniques, based on the separation of hydrogen from its contaminants, and optical techniques, which selectively detect target species through their characteristic optical absorption in solution or gas phase. Gas Chromatography (GC) represents the most widely used analytical technique for the detection of hydrogen impurities [22,23]. In GC, the sample is injected into a separation column, where the various components are separated according to differences in their molecular size, polarity, and interaction with the stationary phase. As a result, each compound is eluted from the column at a distinct retention time, allowing for their individual detection. GC is usually coupled with a mass spectrometer (MS), which basically quantifies the various components at the GC exit. In contrast, optical gas detection techniques offer a non-destructive alternative and are widely used for the analysis of contaminants in gaseous mixtures [24–26]. These techniques can be grouped in two different classes: direct and indirect methods. Direct methods detect contaminants by measuring the light transmitted by the gas sample after the selective optical absorption of specific contaminants, following the well-known Lambert-Beer law, while indirect ones rely on secondary effects arising from light absorption, such as acoustic wave generation or fluorescence. The selection among different technologies involves a trade-off between cost, sensitivity, analysis times, and instrument portability. GC-based methods are highly sensitive but are typically confined to laboratory environments due to their complexity, long analysis times and bulky instrumentation. In contrast, optical techniques, such as cavity ring-down spectroscopy, tunable diode laser spectroscopy, and photoacoustic spectroscopy (PA), enable rapid, non-destructive measurements and are better suited for real-time, in situ monitoring. In this context, Quartz-Enhanced Photoacoustic Spectroscopy (QEPAS) is a promising technique for hydrogen quality monitoring due to its compactness, robustness, small gas sample volume, and suitability for portable and in-field applications [[27]]. The technique has already been successfully applied in environmental monitoring [28], leak detection, and detection of contaminants in natural gas matrices [29], indicating its strong potential for trace impurity detection in different environments. In this work, we propose QEPAS as an indirect optical technique for the real-time detection of CO impurities in hydrogen matrix [30,31]. QEPAS combines high sensitivity and compact design, offering promising solutions for portable and field-deployable instruments [32,33]. In QEPAS, a quartz tuning fork (QTF) is employed as acoustic waves detector, as the laser beam is focused between the QTF prongs, to excite the flexural mode of the QTF itself. Electric charges are produced due to quartz piezoelectricity, generating a signal proportional to the sound wave intensity. For QEPAS sensing, a pair of resonator tubes is acoustically coupled with the QTF. The most popular configuration is the on-beam configuration, where the tubes are located on both sides of the QTF, perpendicular to the prongs plane [34,35]. The tubes are used to enhance the intensity of the acoustic waves up to several tens of times [35], hereby significantly enhancing the overall sensitivity of the QEPAS sensor. A key limitation of QEPAS spectrophones is that the tube geometry is directly determined by the speed of sound in the gaseous sample. Therefore, when moving from standard air to a hydrogen matrix, characterized by a much higher sound speed, the QEPAS spectrophone must be re-designed. For this reason, the first part of this work focuses on the development of a QEPAS spectrophone specifically optimized for contaminants detection in hydrogen, achieved by properly tailoring both the QTF resonance frequency and the acoustic tubes length. The optimized spectrophone was then integrated into a sensor designed to detect trace concentration of CO in H_2, employing a quantum cascade laser (QCL) tuned to the optical transition at 2193.36 cm^{-1}. The QEPAS sensor was calibrated using certified concentrations and its performance was benchmarked against state-of-the-art techniques, to assess the limitations and advantages of the QEPAS technique for impurity monitoring in hydrogen.

Table 1
Hydrogen quality requirements defined by ISO 14687, which specify the maximum permissible concentrations of various contaminants for use in fuel cell road vehicles, in part-per-million (ppm).

Compound	Max (ppm)	Compound	Max (ppm)
Helium (He)	300	Other hydrocarbons	2
Nitrogen (N_2)	300	Formaldehyde (HCHO)	0.2
Argon (Ar)	300	Carbon monoxide (CO)	0.2
Methane (CH_4)	100	Ammonia (NH_3)	0.1
Water vapor (H_2O)	5	Total sulfur compound	0.004
Oxygen (O_2)	5	Total halogenated compounds	0.05
Carbon dioxide (CO_2)	2	Solid particulates	1 (mg/kg)

2. Assembling of the spectrophone for impurities detection in H_2

The model used to account for the enhancement of the acoustic field in the vicinity of the QTF assumes that the tube behaves as an open-ended cylindrical resonator with walls thin enough to be considered negligible [36]. Because of the coupling between the QTF and the tubes, the Q-factor of the spectrophone is reduced compared to the bare QTF, since the tubes are less efficient acoustic resonators. However, this Q-factor loss is compensated by the amplification of the acoustic wave, resulting in an increased QEPAS signal. The optimized distance between the tube-end and the QTF prong is approximately 150-200 μm [37]. The optimal length of the tubes l can be calculated using the open-end correction model [38]:

$$l = \frac{v_s}{2f} - \frac{16a}{3\pi} \quad (1)$$

where v_s is the speed of sound (1220 m/s in hydrogen), a is the internal diameter and f is the QTF resonance frequency, namely that of the sound wave propagating in the tubes. Adopting custom QTFs reported in the literature with a resonance frequency at the fundamental mode of ~15 kHz, commonly employed for environmental monitoring applications in air matrix [35], would require acoustic tubes longer than 38 mm when operating the spectrophone in a hydrogen matrix. Such long tubes would make the optical alignment of the laser beam through the tubes and the QTF prongs critically challenging. The optimal resonator tube length was determined using directly the open-end correction model (Eq. (1)). By imposing a maximum tube length of 15 mm, as typically employed for spectrophones operating in air or nitrogen matrices and considering a sound velocity of 1220 m/s and an internal radius of 1.59 mm, a minimum QTF resonance frequency of ~35 kHz is obtained. Among the custom QTF designs reported in the literature that meet this requirement [35,39], we selected the QTF featuring rectangular prongs proposed in Ref. [40], whose main geometrical parameters are listed in Table 2.

Note that the overtone resonance frequency reported in Table 2 is a theoretical value and has been used as reference value to guide the experimental frequency characterization of the spectrophone. The QEPAS spectrophone was then assembled by coupling this QTF with two resonator tubes having diameter $a = 1.59$ mm and length $l = 1.1$ cm each

Table 2
Main geometrical dimensions and resonance frequencies of the custom QTF design adopted in this work, originally proposed in Ref. [40].

Prong length (mm)	Prong thickness (mm)	Prong width (mm)	Fundamental mode (Hz)	First overtone mode (Hz)
10	0.9	0.25	7205.0	43,950

(as calculated by using Eq. (1) and imposing $f = 44$ kHz). The spectrophone was mounted into a stainless-steel cell with optical windows (ADM01 by Thorlabs) [41] to isolate it from the external environment and to allow the use of pure hydrogen matrix.

The response of the spectrophone at different frequencies was reconstructed around the expected resonance frequency of the first overtone mode (see Table 2). Fig. 1 shows the resonance curves of the first overtone mode, measured in air first and then in pure hydrogen, at atmospheric pressure.

A Lorentzian fit was applied to extract both the frequency and the Q-factor of the spectrophone, even though the curves exhibited slight asymmetry due to the effect of parasitic capacitance, and the extracted values are summarized in Table 3.

In QEPAS sensors, matrix composition variations primarily affect measurement accuracy through changes in the resonance properties of the tuning fork, since resonance frequency and quality factor depend on gas density and viscosity of the surrounding medium [42]. Changes in the background gas composition can therefore alter the QEPAS signal amplitude even at constant target gas concentration. Monitoring the resonance parameters of the spectrophone can thus provide a method to detect matrix variations and apply appropriate signal corrections, improving measurement accuracy. Selectivity, on the other hand, is mainly determined by the spectroscopic properties of the target gas and by the selection of isolated absorption lines. To gain deeper insight into the variations in the resonance properties of the spectrophone under different environments, a systematic analysis was performed over a range of pressure values using pure hydrogen as carrier gas. The ADM was connected to an integrated flow rate and pressure controller (MCQ Instruments, GM Vacuum 1.3) calibrated for operation with hydrogen matrices. To prevent gas stagnation and accumulation, the acquisitions were performed at a gas flow rate of 100 sccm. Fig. 2a shows the QTF resonance profiles measured at different pressures, illustrating both the progressive shift of the resonance peak toward lower frequencies and its broadening as the pressure increases. The dependence of the quality factor on the hydrogen pressure is reported in Fig. 2b. Q-factor decreases with increasing pressure, as evidenced by the broadening of the resonance curves and the reduction in their peak amplitudes. The behavior of the Q-factor of a spectrophone as a function of pressure can be effectively described by introducing two parameters [39,43]. The first, Q_0 , represents the intrinsic quality factor of the QTF, i.e., the contribution associated with loss contribution independent of pressure, such as those arising from the support or internal dissipation mechanisms [44]. Conversely, the reaction force exerted by the gas as the prongs vibrate leads to additional energy losses. If the viscous force of the gas is assumed as the only source of damping, a damping parameter a can be introduced that relates the pressure-dependent energy loss contribution to the gas pressure [45,46]. Under these assumptions, the dependence of the Q-factor on operating pressure can be modeled according to the following relation [47]:

$$Q = \frac{Q_0}{1 + Q_0 a\sqrt{P}} \tag{2}$$

The data in Fig. 2a were fitted using Eq. (2), yielding a damping parameter of $a = 5.58 \cdot 10^{-7}$ Torr$^{-0.5}$. This value is approximately one order of magnitude lower than that typically observed for QTFs operated inside air samples [43].

This result is consistent with expectations, as the energy loss can be qualitatively correlated with the molar mass of the surrounding molecules: the lower the molar mass, the lower the expected damping. Therefore, the reaction force exerted by hydrogen molecules is weaker than that in air, leading to higher Q-factor values (see Table 3). Consistent conclusions can be drawn from the linearly dependent variation of the resonance frequency on hydrogen pressure, shown in Fig. 3c. When the spectrophone operates in a viscous medium, the fluid-structure interaction can be described by introducing an added mass to the prong, primarily determined by the molar mass of the surrounding gas molecules [47,48]. As a result, the resonance frequency f reduces with the pressure P following a linear trenddescribed by the relation $f=f_0-kP$, where f_0 represents the theoretical resonance frequency in vacuum. The linear fit shown in Fig. 3c gives a slope of $k = 0.99$ mHz/Torr, which is smaller than the values typically reported for similar QTFs operating in air, as expected [43].

3. Quartz-enhanced photoacoustic detection of CO impurities in H_2

Following the spectrophone characterization, the ADM and the gas line management system were integrated to develop a QEPAS sensor, whose schematic layout is shown in Fig. 3.

The light source employed was a DFB-QCL by ADTECH OPTICS, with an emission wavelength of $\lambda = 4.57$ μm, operated at a temperature of 12 °C to target CO absorption line at 2193.36 cm^{-1} with an absorption cross section of 1.1*10^{-18} cm^2/mol at T = 25°, P = 1 atm, obtained using H_2 as buffer gas [49]. The current supply and temperature control of the DFB-QCL were managed using a controller (Thorlabs ITC4002QCL), in combination with an external water-cooled chiller to ensure stable thermal conditions. A plane-convex lens (Thorlabs LA5042-E1, f = 75 mm) with anti-reflection coating in the 2-5 μm range was used to focus the laser beam in the QEPAS spectrophone. A power-meter was positioned after the exit window of the ADM for alignment purposes. For QEPAS measurements, the light was modulated at half of the first overtone frequency of the spectrophone by applying a sinusoidal modulation to laser injection current, while a slow 10 mHz-ramp signal was simultaneously applied to scan across the CO absorption line. Both modulations were generated by a waveform generator (WFG, Tektronix AFG31052), and the sinusoidal modulation

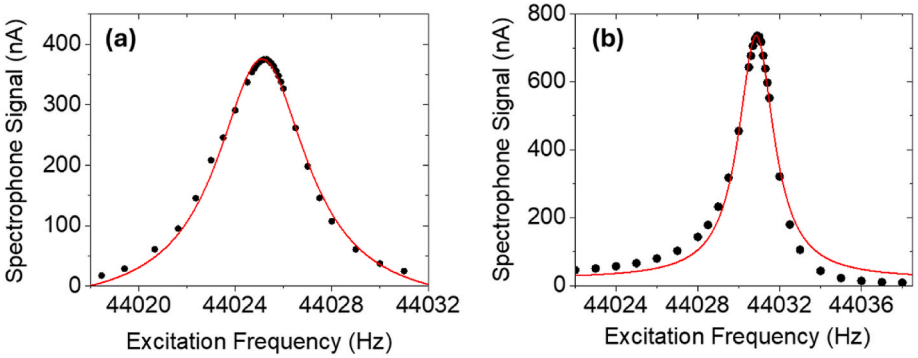

Fig. 1. Resonance curves (data points) of the spectrophone operating at the first overtone, measured at atmospheric pressure in air (a) and in pure hydrogen (b). The red lines represent Lorentzian fit to the experimental data. (For interpretation of the references to colour in this figure legend, the reader is referred to the Web version of this article.)

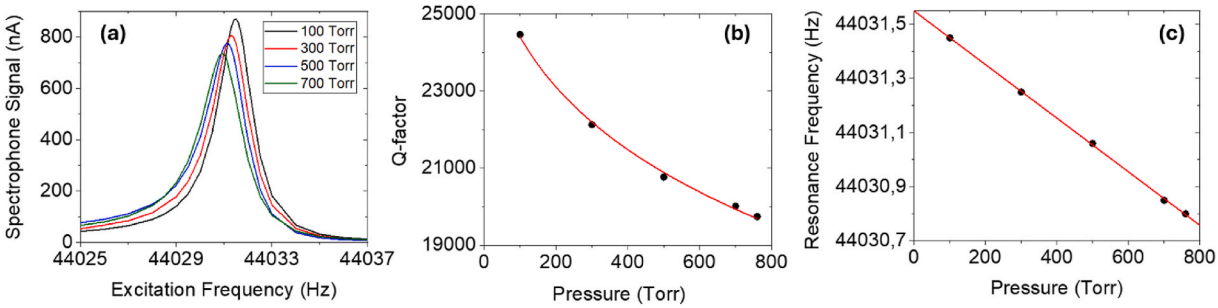

Fig. 2. (a) Resonance curves of the spectrophone excited at the first overtone mode measured at different gas pressures (100, 300, 500, and 700 Torr) in pure hydrogen, showing the progressive frequency shift and broadening due to viscous damping. (b) Variation of the spectrophone quality factor with gas pressure and best fit using Eq. (2) (red curve). (c) Resonance frequency of the spectrophone as a function of pressure and best linear fit to the experimental data (red line). (For interpretation of the references to colour in this figure legend, the reader is referred to the Web version of this article.)

Table 3
Resonance frequency and quality factor of the spectrophone when operating at the QTF first overtone mode in air and in hydrogen. The values are obtained from the Lorentzian fits of the data shown in Fig. 2.

Matrix	Resonance frequency (Hz)	Q-factor
Air	44024.1 Hz	9700
Hydrogen	44030.9 Hz	19740

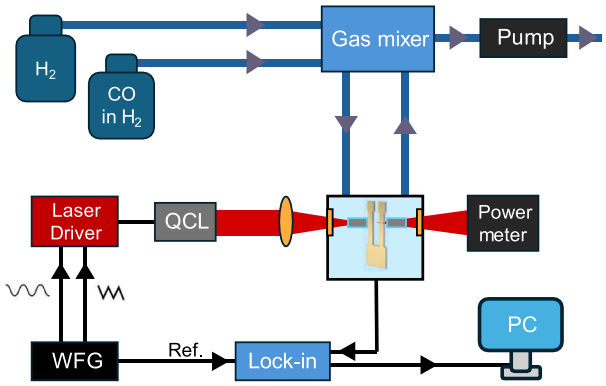

Fig. 3. Experimental setup of the QEPAS sensor for CO detection in hydrogen. The QCL beam is aligned through the resonator tubes and between the QTF prongs. A power meter is positioned downstream for optical alignment. A gas mixer and a pump allowed to create mixtures with different concentrations of CO within H_2 matrix, starting from a cylinder containing a certified 1000 ppm CO in H_2 mixture and a cylinder with pure H_2. WFG: Waveform Generator; QCL: Quantum Cascade Laser.

was simultaneously used as the reference for the lock-in amplifier (Zurich Instruments MFLI), which demodulates the signal at the second harmonic following the WM–2f detection scheme. To calibrate the QEPAS sensor, two cylinders with certified concentration of pure H_2 (6.0) and 800 ppm of CO:H_2, respectively, were connected to the GM Vacuum 1.3 (MCQ Instruments), employed as gas mixer.

3.1. Optimization of the sensor operating conditions

Both the optimal working pressure and the laser current modulation were determined to identify the conditions that maximize the QEPAS signal amplitude. Five different pressures were investigated, and for each pressure the modulation amplitude was varied to evaluate the corresponding QEPAS peak signal obtained by reconstructing the spectral scan of the targeted CO absorption line. All spectra were recorded by introducing into the ADM a certified gas mixture containing 800 ppm of CO in H_2 at a constant flow rate of 50 sccm. The QEPAS peak amplitudes (S) were normalized to the maximum recorded signal (2.6 nA, obtained at 700 Torr with a modulation amplitude of 110 mVpp) and are shown in Fig. 4a as a function of the modulation amplitude.

The experimental conditions yielding the best performance were identified as a gas pressure of 700 Torr and a modulation amplitude of 110 mVpp; these parameters were consequently selected for the sensor calibration discussed in the following section. Increasing the operating pressures, the range of modulation amplitude values that maximize the QEPAS signal also increases. This effect is a direct consequence of the pressure broadening of the CO absorption line, which requires a larger wavelength modulation to fully scan across the broadened absorption feature. Fig. 4b shows the QEPAS peak amplitudes as a function of the sample pressure; each data point was recorded using the optimal modulation amplitude determined from the analysis in Fig. 4a.

3.2. Sensor calibration and minimum detection limit

After identifying the operating conditions that maximize the QEPAS response, the sensor calibration was carried out. A certified gas cylinder containing 800 ppm of CO in H_2 was diluted with high-purity hydrogen to obtain mixtures at different CO concentrations. For each concentration level, a 2f-QEPAS spectral scan of the selected CO absorption feature was acquired, and the corresponding peak amplitude was extracted. The recorded spectra and the resulting calibration curve are presented in Fig. 5a and b, respectively.

With intercept value lower than the noise level, the slope of the linear fit, giving the sensitivity of the CO QEPAS sensor, resulted 3.36 ± 0.07 pA/ppm.

The most important figure of merit, especially for comparison with other types of sensors, is the minimum detectable limit (MDL), usually defined as the concentration corresponding to a signal equal to the noise level, i.e., when the Signal-to-Noise Ratio (SNR) is equal to one. Based on the average sensitivity and a 1σ noise level of 30 pA, a MDL of 8.9 ppm was obtained for an integration time of 100 ms. Although longer integration times can, in principle, further lower the MDL through increased averaging, an optimal averaging time typically exists at which the detection limit reaches its minimum. Beyond this optimum, the sensor performance degrades, mainly due to low-frequency drifts induced by mechanical vibrations. To evaluate this effect, an Allan variance analysis of the noise signal was carried out in order to determine the MDL as a function of the integration time.

During this measurement, the QCL wavelength was locked to the center of the CO absorption feature while pure H_2 was continuously flowed through the QEPAS setup. The corresponding Allan–Werle deviation curve is reported in Fig. 6.

As shown, the Allan–Werle plot exhibits the expected Johnson noise behavior, decreasing proportionally to $1/\sqrt{t}$ for integration times up to 10 s. [50,51]. The rise in the noise standard deviation at longer integration times is attributed to slow mechanical oscillations. For an

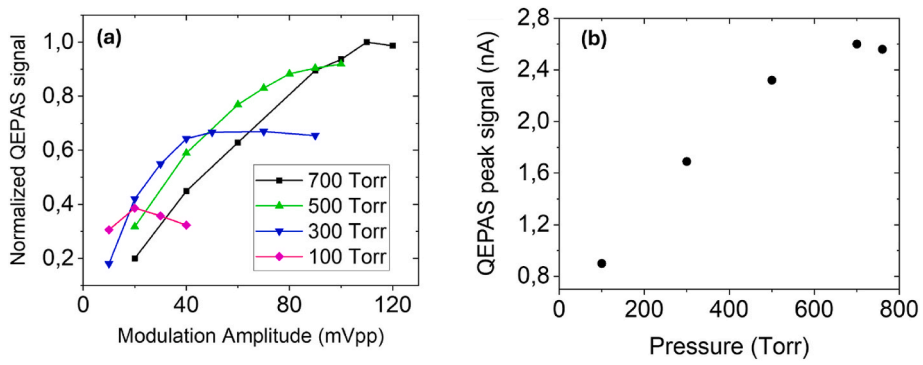

Fig. 4. (a) QEPAS peak signal, normalized to its maximum value, plotted versus the modulation amplitude applied to the QCL current driver. The measurements were carried out by flowing a certified gas mixture of 800 ppm CO in H_2 through the ADM at 50 sccm. The dataset acquired at 760 Torr is not displayed because it largely overlaps with the curve obtained at 700 Torr. (b) Dependence of the QEPAS peak signal on the gas pressure. For each pressure value, the modulation amplitude corresponding to the maximum QEPAS response, identified from panel (a), is employed.

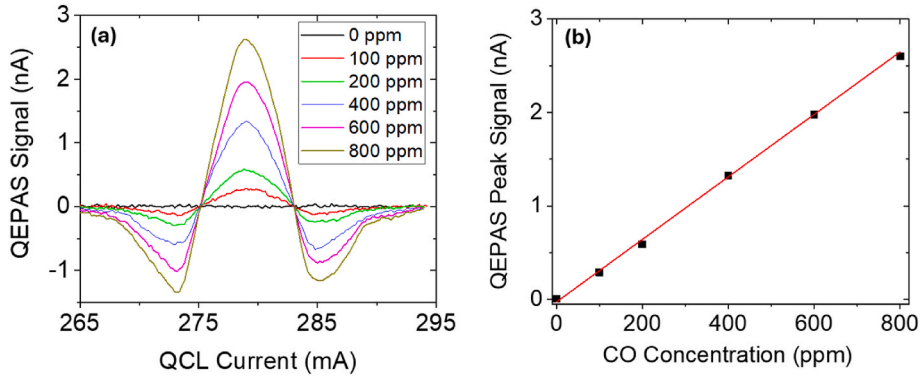

Fig. 5. (a) 2f-QEPAS spectra measured at various CO concentrations, generated by diluting a certified 800 ppm CO in H_2 mixture with high-purity hydrogen. (b) QEPAS peak amplitude plotted versus CO concentration (black markers), together with the corresponding linear regression fit (solid red line). (For interpretation of the references to colour in this figure legend, the reader is referred to the Web version of this article.)

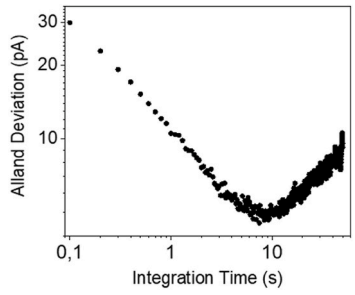

Fig. 6. Allan–Werle deviation plot of the CO QEPAS sensor. The signal was monitored with the QCL wavelength fixed at the maximum of the CO absorption line, while pure H_2 was continuously introduced into the ADM at a flow rate of 50 sccm.

integration time of 1 s, the measured deviation is $\sigma_{1s} = 10.5$ pA, corresponding to an MDL of 3.0 ppm, which decreases to 1.5 ppm when the integration time is extended to 10 s.

4. Measurement of relaxation rate of CO in H_2 matrix

According to the theoretical framework of QEPAS, the generated signal is proportional to the spectrophone quality factor and the radiation-to-sound conversion efficiency, $\varepsilon(P)$; both of these parameters depend on the specific gas matrix used [52].

As discussed above, the spectrophone quality factor, $Q(P)$, is primarily influenced by energy losses arising from collisions with the surrounding gas, which are in turn dependent on the molecular weight of the gas matrix. In contrast, the radiation-to-sound conversion efficiency quantifies how efficiently sound waves are generated and transmitted following the optical excitation of target molecule. When photons are absorbed and a fundamental vibrational mode is excited, the molecule can relax either radiatively, by emitting a photon, or non-radiatively, through collisions with neighboring molecules. The latter pathway dominates and can be described using Landau's model. Considering vibrational transitions $\nu(1 \rightarrow 0)$ occurring during molecular collisions, the populations of the vibrational states $\nu = 0$ and $\nu = 1$ follow a Boltzmann distribution. The characteristic lifetime, τ, is inversely proportional to the collision rate, k, and corresponds to the vibrational-to-translational (V–T) relaxation time that is the average time required for a molecule to convert its vibrational energy into kinetic energy via collisions [52].

Because both ε and Q vary with gas pressure, studying the pressure dependence of the QEPAS signal can provide information about the efficiency of acoustic wave generation and propagation in the hydrogen matrix. This, in turn, enables the determination of the effective non-radiative relaxation rate of CO molecules within the hydrogen matrix. Under the simplest assumption, where only V–T relaxation from the excited to the ground vibrational state takes place, the radiation-to-sound conversion efficiency can be expressed as [53,54]:

$$\varepsilon(P) = \frac{1}{\sqrt{1 + \left(\frac{2\pi f}{kP}\right)^2}} \propto \frac{S(P)}{Q(P)} \tag{3}$$

In Fig. 4b, the QEPAS signal is shown as a function of the gas pressure. The observation of a pressure value that maximizes the signal reflects a trade-off between two competing effects. As the pressure increases, the Q-factor decreases (as experimentally observed through the electrical excitation of the spectrophone, see Fig. 2b), whereas the radiation-to-sound conversion efficiency is expected to rise due to the greater number of molecular available for collisions, thereby enhancing the translational energy transfer among molecules. Based on the previous analysis, the ratio *S(P)/Q(P)* provides an estimate of the pressure dependence of the radiation-to-sound conversion efficiency, $\varepsilon(P)$. Therefore, the ratio between the data points shown in Figs. 4b and 2b was calculated for each pressure value, normalized to the maximum value, and subsequently fitted using Eq. (3). The fitting result is presented in Fig. 7.

The fitting parameter $B = \frac{2\pi f}{k}$ has an explicit dependence on the relaxation rate of CO molecules on the hydrogen matrix, and it results B=631.37±114.99 $Torr^{-1}$. Considering the operating frequency f = 44030.8 Hz, the relaxation rate $k_{CO\text{-}H2}$ of CO molecules on the hydrogen matrix results $k_{CO\text{-}H2}$=438.0±80 $s^{-1}Torr^{-1}$.

5. Comparison with state-of-the-art photoacoustic detection

This section presents a comparison between the relaxation rate of CO in a hydrogen matrix and that of the same molecule in nitrogen, followed by a comparison between ammonia (NH_3) and CO in the same hydrogen matrix. For a meaningful comparison, only the CO QEPAS sensor operating in air, on the same absorption line and with comparable optical power and exhibiting among the best performance reported in the literature, was considered to isolate the effect of the background gas matrix [55]. Comparing the non-radiative relaxation rates of CO in different gas matrices allows one to assess how effectively each matrix converts the vibrational energy of optically excited CO molecules into translational energy, which in turn determines the efficiency of sound wave generation in the gas. Fig. 8a illustrates the variation of the S/Q ratio with gas pressure for CO in a N_2 matrix, using data reported for a CO QEPAS sensor in Ref. [56], along with the best fit using Eq. (3).

It is worth noting that the CO vibrations were excited on the same absorption line used in the present study. The main difference is the use of a spectrophone equipped with a QTF of lower resonance frequency, which is necessary due to the difference in the speed of sound between the two gas matrices. For a comprehensive comparison, the same analysis was applied to NH_3 in H_2 using the data reported in Ref. [57]. This approach allows for the estimation of the effective relaxation rate of NH_3 in H_2. The results are presented in Fig. 8b. A summary of the effective V–T relaxation rates extracted for different gas mixtures is reported in Table 4. The table includes the measured relaxation rates together with the corresponding spectrophone operating frequencies for each target species and gas matrix.

A first comparison, aimed at understanding the role of optically active species, involves carbon monoxide and ammonia in the same hydrogen matrix. The effective relaxation rate found for NH_3 is approximately three times higher than that of CO, indicating that ammonia relaxes more rapidly. This behavior, previously observed in a nitrogen matrix, is thus confirmed in a hydrogen matrix as well [58]. A comparison of the effective relaxation rates for CO in N_2 and H_2 reveals no substantial differences, as the extracted values are of the same order of magnitude. This result can be explained by considering that the effective V–T relaxation rate depends on both the collision frequency and the energy transfer efficiency per collision. Hydrogen, due to its low molecular mass, leads to higher molecular velocities and therefore higher collision frequencies, but a lower energy transfer efficiency per collision because of the unfavorable mass ratio. Nitrogen, on the other hand, being heavier, provides more efficient vibrational-to-translational energy transfer despite lower collision rates. These competing effects partially compensate each other, resulting in similar effective relaxation rates in the two gas matrices. Despite the similarity in the effective relaxation rates, a substantial difference emerges in the MDLs. For an integration time of 1s, the MDL of CO in the hydrogen matrix is 3.0 ppm, while in the nitrogen matrix it reaches 12 ppb [55]. A similar comparison can be made for NH_3. The MDL reported in a nitrogen matrix is 6.0 ppb [59], whereas it reaches 95 ppb in a hydrogen matrix, with both measurements were conducted with an integration time of 100 ms, using the same absorption line at 9.06 μm and comparable optical power. This discussion proves that the modulation frequency is a key parameter when the spectrophone operates in hydrogen. Due to the higher speed of sound, the spectrophone must operate at higher resonance frequencies, which implies higher modulation frequencies. In the frequency-domain photoacoustic model, the periodic heating produced by modulated optical absorption leads to a pressure wave whose amplitude and phase depend on the relaxation dynamics of the excited molecules. The solution of the heat equation with a finite relaxation time shows that the amplitude of the generated acoustic wave is proportional to $1/\sqrt{1+(2\pi f/k)^2}$, while a phase lag $\phi = \arctan(2\pi f/k)$ is introduced between the optical excitation and the pressure wave [52]. When the modulation frequency becomes comparable to or higher than the V-T relaxation rate (as for CO), a phase lag is introduced between the optical excitation and the thermalization process responsible for pressure wave generation. Under these conditions, the system operates in a relaxation-limited regime rather than absorption-limited, and the photoacoustic signal amplitude depends on the parameter f/k rather than only on the relaxation rate. In this regime, increasing the modulation frequency reduces the efficiency of radiation-to-sound conversion even when the relaxation rate remains unchanged. This effect is particularly relevant for slow-relaxing molecules such as CO and explains why higher modulation frequencies required in hydrogen lead to higher detection limits compared to nitrogen-based matrices.

The high speed of sound in hydrogen requires the use of higher excitation frequencies in order to employ resonator tubes of practical length while maintaining efficient sound amplification. For both NH_3 and CO in H_2, this requirement results in operating resonance frequency that iseven higher than that of the standard 32.7 kHz QTF. Although this tuning fork was widely used in early QEPAS implementations, it was later abandoned because several studies showed that this frequency is too high, namely too fast for gases characterized by a slow relaxation process, such as CO. It is worth emphasizing that the spectrophone geometry is primarily determined by the acoustic properties of the carrier gas rather than by the specific target impurity. In particular, the resonator tube length is defined by the sound velocity in the gas matrix and by the QTF resonance frequency through the open-end correction model (Eq. (1)). When impurities are present at trace levels, they do not significantly affect the speed of sound in the hydrogen matrix. Therefore, the spectrophone developed in this work is not limited to CO detection but can be extended to other impurity species in hydrogen without requiring a redesign of the acoustic resonator. Multi-species detection in hydrogen with QEPAS technique is therefore feasible,

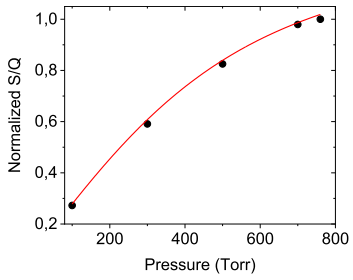

Fig. 7. Normalized ratio between CO QEPAS peak signal and spectrophone quality factor (S/Q) plotted versus gas pressure. The red line represents the best fit according to Eq. (3). (For interpretation of the references to colour in this figure legend, the reader is referred to the Web version of this article.)

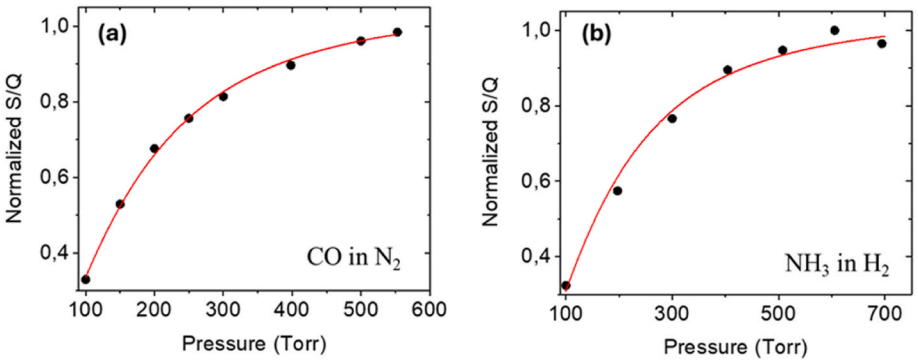

Fig. 8. (a) S/Q data normalized to the unity as a function of pressure (in Torr) for CO in N_2 using data reported in Ref. [56]. (b) S/Q data normalized normalized to the unity as a function of pressure (in Torr) for NH_3 in H_2 using data reported in Ref. [57]. For both panels, the red curve is the best fit of data-points using Eq. (3). (For interpretation of the references to colour in this figure legend, the reader is referred to the Web version of this article.)

Table 4
Effective relaxation rates obtained from the fitting results shown in Figs. 7, 8a and 8b, along with the corresponding spectrophone resonance frequencies, for three different target species–matrix gas mixtures.

Target Species: Matrix	Effective Relaxation Rate (s^{-1} $Torr^{-1}$)	Frequency (Hz)
CO:N_2	359.0 ± 34.6	12445.10
CO:H_2	438 ± 80	44030.85
NH_3:H_2	1164.3 ± 238.6	44135.69

provided that appropriate and sufficiently strong absorption lines are selected and that they are spectrally isolated within the laser tuning range to avoid spectral overlapping. Therefore, cross-sensitivity is primarily a spectroscopic issue rather than an acoustic one. To further substantiate this discussion, the results obtained in this work for CO detection in H_2 are compared with those achieved using traditional PAS by C. Feng et al., under nearly identical experimental conditions in terms of laser source parameters, i.e., excitation wavelength and optical power [60]. In their study, a differential photoacoustic cell was used to detect CO impurities in hydrogen. Various CO concentrations, diluted in pure hydrogen, were introduced into the cell to verify the linearity of the PAS signal with concentration, achieving a minimum detection limit (MDL) of 8 ppb with a 1 s integration time. This performance is comparable to the best MDL reported for QEPAS detection of CO in N_2, which is 12 ppb at a resonance frequency of approximately 12.45 kHz. [55]. In the PAS configuration reported by C. Feng et al. the fundamental resonance frequency was 7049 Hz, which is about 6.2 times lower than the first overtone mode of spectrophone used in this work. This substantially higher resonance frequency is therefore the main reason for the lower MDL obtained in the present QEPAS setup. One possible solution would be to use a QTF with a lower operating frequency or to exploit the fundamental mode of QTF. However, as discussed above, lowering the resonance frequency would require significantly longer acoustic resonator tubes. For instance, operating at *f=12.45 kHz* would result in an optimized tube length of 46.3 mm, nearly four times longer than the resonators used in the present work. However, such a configuration would make optical alignment considerably more challenging, especially when employing laser sources with limited spatial beam quality. Despite this limitation, QEPAS retains key advantages over conventional PAS and cavity-based optical sensors, notably its inherently compact architecture and extremely small effective sample volume. These features enable reduced gas consumption, faster response times, and straightforward integration into portable and in-field systems. As a result, QEPAS represents a favorable compromise between sensitivity and practicality, especially for applications where compactness and low sample volume are critical requirements.

6. Conclusions

This work presented the design, optimization, and experimental validation of a QEPAS sensor for the detection of CO impurities in a hydrogen matrix. A custom spectrophone operating at ~44 kHz was specifically designed to compensate for the high speed of sound in hydrogen while maintaining compact resonator dimensions and efficient acoustic coupling. The sensor achieved a minimum detection limit of 3.0 ppm with 1 s integration time, demonstrating the feasibility of QEPAS-based trace gas detection in hydrogen environment. Beyond the experimental demonstration, this work provides practical design guidelines for QEPAS spectrophones operating in hydrogen. In particular, it was shown that the spectrophone geometry is primarily determined by the speed of sound in the carrier gas, which imposes higher resonance frequencies compared to standard air or nitrogen-based gas mixtures. This introduces a fundamental trade-off between acoustic resonator dimensions, spectrophone resonance frequency, and sound wave amplification, especially for slow-relaxing molecules. A key result of this work is that the detection limit in hydrogen is not only determined by the intrinsic V–T relaxation rate, but by the ratio between the modulation frequency and the relaxation rate. Due to the higher resonance frequencies required in hydrogen, the system operates in a relaxation-limited regime, which reduces the photoacoustic conversion efficiency even when relaxation rates are comparable to those measured in nitrogen. This finding helps explain the performance differences between QEPAS sensors operating in different gas matrices and represents an important design consideration for future sensors targeting hydrogen quality monitoring. However, compared to conventional photoacoustic cells, QEPAS offers significant advantages in terms of compactness, reduced sample volume, and potential for portable and in-field operation. Although the higher modulation frequency required in hydrogen currently limits the achievable detection sensitivity for slow-relaxing molecules, the results of this work demonstrate that QEPAS remains a promising technique for hydrogen impurity monitoring, particularly where compact and low-volume sensors are required. It should be noted that the minimum detection limit achieved in this work does not yet meet the ISO 14687 requirement for CO concentration in hydrogen. Therefore, the present work should be regarded as a proof-of-concept study and as a set of design guidelines for QEPAS sensors operating in hydrogen environments, rather than as a fully optimized sensor meeting ISO specifications. Further improvements in detection sensitivity could be achieved through several strategies, including the use of lower-frequency QTFs combined with high beam-quality laser sources, alternative spectrophone configurations for increasing the acoustic wave pattern in the resonator tubes, and the extension of the sensing approach to multi-species detection for comprehensive hydrogen quality monitoring.

CRediT authorship contribution statement

Mariagrazia Olivieri: Writing – original draft, Investigation, Formal analysis, Data curation. **Andrea Zifarelli:** Writing – review & editing, Investigation, Formal analysis, Conceptualization. **Giansergio Menduni:** Writing – review & editing, Formal analysis, Data curation. **Enrico Sallustio:** Investigation, Formal analysis, Data curation. **Angelo Sampaolo:** Writing – review & editing, Supervision, Methodology. **Vincenzo Spagnolo:** Writing – review & editing, Supervision, Methodology. **Pietro Patimisco:** Writing – review & editing, Supervision, Methodology, Conceptualization.

Fundings

This research was funded by the PNRR MUR project PE0000023–NQSTI, the MUR "Dipartimenti di Eccellenza 2023–2027" program through the project Quantum Sensing and Modelling for One-Health (QuaSiModO), and by THORLABS GmbH in the framework of the PolySenSe joint research laboratory. Andrea Zifarelli and Pietro Patimisco also acknowledge financial support from the project HIGAS – Development of a Hydrogen Impurity Gas Analyzer based on Quartz-Enhanced Photoacoustic Spectroscopy (D33C22001330002), carried out within the PNRR MUR project PE0000021–NEST, Network 4 "Energy Sustainable Transition".

Declaration of competing interest

The authors declare that they have no known competing financial interests or personal relationships that could have appeared to influence the work reported in this paper.

Data availability

Data will be made available on request.

References

[1] Akpasi SO, Smarte Anekwe IM, Tetteh EK, Amune UO, Mustapha SI, Kiambi SL. Hydrogen as a clean energy carrier: advancements, challenges, and its role in a sustainable energy future. Clean Energy 2025;9:52–88. https://doi.org/10.1093/CE/ZKAE112.
[2] Oliveira AM, Beswick RR, Yan Y. A green hydrogen economy for a renewable energy society. Curr Opin Chem Eng 2021;33:100701. https://doi.org/10.1016/J.COCHE.2021.100701.
[3] Maka AOM, Mehmood M. Green hydrogen energy production: current status and potential. Clean Energy 2024;8:1–7. https://doi.org/10.1093/CE/ZKAE012.
[4] Moritz M, Schönfisch M, Schulte S. Estimating global production and supply costs for green hydrogen and hydrogen-based green energy commodities. Int J Hydrogen Energy 2023;48:9139–54. https://doi.org/10.1016/J.IJHYDENE.2022.12.046.
[5] Mazloomi K, Gomes C. Hydrogen as an energy carrier: prospects and challenges. Renew Sustain Energy Rev 2012;16:3024–33. https://doi.org/10.1016/J.RSER.2012.02.028.
[6] Shadidi B, Najafi G, Yusaf T. A review of hydrogen as a fuel in internal combustion engines. Energies 2021 2021;14:14. https://doi.org/10.3390/EN14196209.
[7] Hosseini SE, Wahid MA. Hydrogen production from renewable and sustainable energy resources: promising green energy carrier for clean development. Renew Sustain Energy Rev 2016;57:850–66. https://doi.org/10.1016/J.RSER.2015.12.112.
[8] Mitsushima VH and S. Fuel cells and hydrogen. Elsevier; 2018. https://doi.org/10.1016/C2016-0-01053-7.
[9] Buttner WJ, Post MB, Burgess R, Rivkin C. An overview of hydrogen safety sensors and requirements. Int J Hydrogen Energy 2011;36:2462–70. https://doi.org/10.1016/j.ijhydene.2010.04.176.
[10] Sopian K, Wan Daud WR. Challenges and future developments in proton exchange membrane fuel cells. Renew Energy 2006;31:719–27. https://doi.org/10.1016/j.renene.2005.09.003.
[11] Stöhr T, Reiter V, Scheikl S, Klopčič N, Brandstätter S, Trattner A. Hydrogen quality in used natural gas pipelines: an experimental investigation of contaminants according to ISO 14687:2019 standard. Int J Hydrogen Energy 2024;67:1136–47. https://doi.org/10.1016/J.IJHYDENE.2023.09.305.
[12] Du Z, Liu C, Zhai J, Guo X, Xiong Y, Su W, et al. A review of hydrogen purification technologies for fuel cell vehicles. Catal 2021;11(11):1–19. https://doi.org/10.3390/CATAL11030393.
[13] Wang X, Baker P, Zhang X, Garces HF, Bonville LJ, Pasaogullari U, et al. An experimental overview of the effects of hydrogen impurities on polymer electrolyte membrane fuel cell performance. Int J Hydrogen Energy 2014;39:19701–13. https://doi.org/10.1016/J.IJHYDENE.2014.09.151.
[14] ISO 14687:2025 - Hydrogen fuel quality — product specification. 2025.
[15] Arcos JMM, Santos DMF, Arcos JMM, Santos DMF. The hydrogen color spectrum: techno-economic analysis of the available technologies for hydrogen production. Gas 2023;3:25–46. https://doi.org/10.3390/GASES3010002. 2023;3:25–46.
[16] Majlan EH, Wan Daud WR, Iyuke SE, Mohamad AB, Kadhum AAH, Mohammad AW, et al. Hydrogen purification using compact pressure swing adsorption system for fuel cell. Int J Hydrogen Energy 2009;34:2771–7. https://doi.org/10.1016/J.IJHYDENE.2008.12.093.
[17] Besancon BM, Hasanov V, Imbault-Lastapis R, Benesch R, Barrio M, Mølnvik MJ. Hydrogen quality from decarbonized fossil fuels to fuel cells. Int J Hydrogen Energy 2009;34:2350–60. https://doi.org/10.1016/j.ijhydene.2008.12.071.
[18] Beurey C, Gozlan B, Carré M, Bacquart T, Morris A, Moore N, et al. Review and Survey of methods for analysis of impurities in hydrogen for fuel cell vehicles according to ISO 14687:2019. Front Energy Res 2021;8:615149. https://doi.org/10.3389/FENRG.2020.615149/BIBTEX.
[19] Papadias DD, Ahmed S, Kumar R, Joseck F. Hydrogen quality for fuel cell vehicles - a modeling study of the sensitivity of impurity content in hydrogen to the process variables in the SMR-PSA pathway. Int J Hydrogen Energy 2009;34:6021–35. https://doi.org/10.1016/J.IJHYDENE.2009.06.026.
[20] Murugan A, Brown AS. Review of purity analysis methods for performing quality assurance of fuel cell hydrogen. Int J Hydrogen Energy 2015;40:4219–33. https://doi.org/10.1016/J.IJHYDENE.2015.01.041.
[21] Brown AS, Vargha GM, Downey ML, Hart NJ, Ferrier GG, Hall KI. Methods for the analysis of trace-level impurities in hydrogen for fuel cell applications. 2011.
[22] Bacquart T, Arrhenius K, Persijn S, Rojo A, Auprêtre F, Gozlan B, et al. Hydrogen fuel quality from two main production processes: steam methane reforming and proton exchange membrane water electrolysis. J Power Sources 2019;444:227170. https://doi.org/10.1016/J.JPOWSOUR.2019.227170.
[23] Arrhenius K, Bohlen H, Büker O, Krom I de, Heikens D, Wijk J van, et al. Hydrogen purity analysis: suitability of sorbent tubes for trapping hydrocarbons, halogenated hydrocarbons and sulphur compounds. Appl Sci 2020 2019;10:10. https://doi.org/10.3390/APP10010120.
[24] Hodgkinson J, Tatam RP. Optical gas sensing: a review. Meas Sci Technol 2012;24:012004. https://doi.org/10.1088/0957-0233/24/1/012004.
[25] Sun J, Chang J, Wang C, Shao J. Tunable diode laser absorption spectroscopy for detection of multi-component gas: a review. Appl Spectrosc Rev 2024. https://doi.org/10.1080/05704928.2024.2302608.
[26] Lackner M. Tunable diode laser absorption spectroscopy (TDLAS) in the process industries - a review. Rev Chem Eng 2007;23:65–147. https://doi.org/10.1515/REVCE.2007.23.2.65.
[27] Dai J, Zhang Y, Wang J, Wang C, Wang Y, Tian Q, et al. Simultaneous dissolved gas analysis in transformer oil via time-division-multiplexed quartz-enhanced photoacoustic spectroscopy. Anal Chem 2026;98:4983–94. https://doi.org/10.1021/ACS.ANALCHEM.5C07335.
[28] Olivieri M, Zifarelli A, Sampaolo A, Spagnolo V, Patimisco P. Time-resolved analysis of carbon monoxide emissions from vehicles using a quartz-enhanced photoacoustic sensor. Opt Laser Technol 2025;192:113879. https://doi.org/10.1016/J.OPTLASTEC.2025.113879.
[29] Olivieri M, Menduni G, Giglio M, Sampaolo A, Patimisco P, Wu H, et al. Characterization of H 2 S QEPAS detection in methane-based gas leaks dispersed into environment. Photoacoustics 2023;29:100438. https://doi.org/10.1016/j.pacs.2022.100438.
[30] Matsuda Y, Nakamura S, Tsurumi N, Shimizu T. Adsorption behavior of carbon monoxide at low concentration on the polymer electrolyte fuel cell. ECS Meet Abstr 2014. https://doi.org/10.1149/MA2014-02/21/1255. MA2014-02:1255.
[31] Jiménez S, Soler J, Valenzuela RX, Daza L. Assessment of the performance of a PEMFC in the presence of CO. J Power Sources 2005;151:69–73. https://doi.org/10.1016/J.JPOWSOUR.2005.02.049.
[32] Sampaolo A, Patimisco P, Giglio M, Zifarelli A, Wu H, Dong L, et al. Quartz-enhanced photoacoustic spectroscopy for multi-gas detection: a review. Anal Chim Acta 2021:338894. https://doi.org/10.1016/j.aca.2021.338894.
[33] Ma Y. Review of recent advances in QEPAS-based trace gas sensing. Appl Sci 2018 2018;8:8. https://doi.org/10.3390/APP8101822.
[34] Patimisco P, Sampaolo A, Zheng H, Dong L, Tittel FK, Spagnolo V. Quartz–enhanced photoacoustic spectrophones exploiting custom tuning forks: a review. Adv Phys X 2017;2:169–87. https://doi.org/10.1080/23746149.2016.1271285. ;PAGE:STRING:ARTICLE/CHAPTER.
[35] Patimisco P, Sampaolo A, Giglio M, dello Russo S, Mackowiak V, Rossmadl H, et al. Tuning forks with optimized geometries for quartz-enhanced photoacoustic spectroscopy. Opt Express 2019;27:1401–15. https://doi.org/10.1364/OE.27.001401.
[36] Levine H, Schwinger J. On the radiation of sound from an unflanged circular pipe. Phys Rev 1948;73:383. https://doi.org/10.1103/PhysRev.73.383.
[37] Dello Russo S, Giglio M, Sampaolo A, Patimisco P, Menduni G, Wu H, et al. Acoustic coupling between resonator tubes in quartz-enhanced photoacoustic spectrophones employing a large prong spacing tuning fork. Sensors 2019;19:4109. https://doi.org/10.3390/S19194109.
[38] Ogawa N, Kaneko F. Open end correction for a flanged circular tube using the diffusion process. Eur J Phys 2013;34:1159. https://doi.org/10.1088/0143-0807/34/5/1159.
[39] Patimisco P, Sampaolo A, Mackowiak V, Rossmadl H, Cable A, Tittel FK, et al. Loss mechanisms determining the quality factors in quartz tuning forks vibrating at the fundamental and first overtone modes. IEEE Trans Ultrason Ferroelectrics Freq Control 2018;65:1951–7. https://doi.org/10.1109/TUFFC.2018.2853404.

[40] Wu H, Sampaolo A, Dong L, Patimisco P, Liu X, Zheng H, et al. Quartz enhanced photoacoustic H2S gas sensor based on a fiber-amplifier source and a custom tuning fork with large prong spacing. Appl Phys Lett 2015;107. https://doi.org/10.1063/1.4930995/28307.
[41] Thorlabs - ADM01 Acoustic Detection Module for QEPAS,Hylok fittings, BaF2 Windows n.d. https://www.thorlabs.com/thorproduct.cfm?partnumber=ADM01.
[42] Feng C, Zifarelli A, Menduni G, Sampaolo A, Wu H, Dong L, et al. Low frequency quartz tuning fork as hydrogen sensor. Int J Hydrogen Energy 2024;96:763–70. https://doi.org/10.1016/J.IJHYDENE.2024.11.365.
[43] Patimisco P, Sampaolo A, Dong L, Giglio M, Scamarcio G, Tittel FK, et al. Analysis of the electro-elastic properties of custom quartz tuning forks for optoacoustic gas sensing. Sensor Actuator B 2016;227:539–46. https://doi.org/10.1016/j.snb.2015.12.096.
[44] Hao Z, Erbil A, Ayazi F. An analytical model for support loss in micromachined beam resonators with in-plane flexural vibrations. Sensors Actuators, A Phys 2003;109:156–64. https://doi.org/10.1016/j.sna.2003.09.037.
[45] Hosaka H, Itao K, Kuroda S. Damping characteristics of beam-shaped micro-oscillators. Sensors Actuators, A Phys 1995;49:87–95. https://doi.org/10.1016/0924-4247(95)01003-J.
[46] Aoust G, Levy R, Bourgeteau B, Le Traon O. Acoustic damping on flexural mechanical resonators. Sensors Actuators A Phys 2016;238:158–66. https://doi.org/10.1016/J.SNA.2015.12.011.
[47] Olivieri M, Zifarelli A, Menduni G, Di Gioia M, Marzocca C, Passaro VMN, et al. Influence of air pressure on the resonance properties of a t-shaped quartz tuning fork coupled with resonator tubes. Appl Sci 2021;11. https://doi.org/10.3390/app11177974.
[48] Christen M. Air and gas damping of quartz tuning forks. Sensor Actuator 1983;4:555–64. https://doi.org/10.1016/0250-6874(83)85067-7.
[49] Kochanov RV, Gordon IE, Rothman LS, Wcisło P, Hill C, Wilzewski JS. HITRAN application programming interface (HAPI): a comprehensive approach to working with spectroscopic data. J Quant Spectrosc Radiat Transf 2016;177:15–30. https://doi.org/10.1016/J.JQSRT.2016.03.005.
[50] Giglio M, Patimisco P, Sampaolo A, Scamarcio G, Tittel FK, Spagnolo V. Allan deviation plot as a tool for quartz-enhanced photoacoustic sensors noise analysis. IEEE Trans Ultrason Ferroelectrics Freq Control 2016;63:555–60. https://doi.org/10.1109/TUFFC.2015.2495013.
[51] Dong L, Kosterev AA, Thomazy D, Tittel FK. QEPAS spectrophones: design, optimization, and performance. Appl Phys B 2010;100:627–35. https://doi.org/10.1007/s00340-010-4072-0.
[52] Müller M, Rück T, Jobst S, Pangerl J, Weigl S, Bierl R, et al. An algorithmic approach to compute the effect of non-radiative relaxation processes in photoacoustic spectroscopy. Photoacoustics 2022;26:100371. https://doi.org/10.1016/j.pacs.2022.100371.
[53] Dello Russo S, Sampaolo A, Patimisco P, Menduni G, Giglio M, Hoelzl C, et al. Quartz-enhanced photoacoustic spectroscopy exploiting low-frequency tuning forks as a tool to measure the vibrational relaxation rate in gas species. Photoacoustics 2021;21:100227. https://doi.org/10.1016/j.pacs.2020.100227.
[54] Olivieri M, Giglio M, Dello Russo S, Menduni G, Zifarelli A, Patimisco P, et al. Assessment of vibrational-translational relaxation dynamics of in a wet-nitrogen matrix through QEPAS. Photoacoustics 2023;31:100518. https://doi.org/10.1016/j.pacs.2023.100518.
[55] Sgobba F, Sampaolo A, Patimisco P, Giglio M, Menduni G, Ranieri AC, et al. Compact and portable quartz-enhanced photoacoustic spectroscopy sensor for carbon monoxide environmental monitoring in urban areas. Photoacoustics 2022;25:100318. https://doi.org/10.1016/j.pacs.2021.100318.
[56] De Palo R, Elefante A, Biagi G, Paciolla F, Weih R, Villada V, et al. Quartz-enhanced photoacoustic sensors for detection of eight air pollutants. Adv Photonics Res 2023;4:1–11. https://doi.org/10.1002/adpr.202200353.
[57] Feng C, Cui R, Menduni G, Zifarelli A, Patimisco P, Sampaolo A, et al. Detection of NH3 impurities in H2 environment exploiting quartz-enhanced photoacoustic spectroscopy with an optimized spectrophone. https://doi.org/10.1016/j.snb.2025.137488; 2025.
[58] Li S, Dong L, Wu H, Sampaolo A, Patimisco P, Spagnolo V, et al. Ppb-level quartz-enhanced photoacoustic detection of carbon monoxide exploiting a surface grooved tuning fork. Anal Chem 2019;91:5834–40. https://doi.org/10.1021/acs.analchem.9b00182.
[59] Menduni G, Zifarelli A, Kniazeva E, Russo S Dello, Ranieri AC, Ranieri E, et al. Measurement of methane, nitrous oxide and ammonia in atmosphere with a compact quartz-enhanced photoacoustic sensor. Sens Actuators, B Chem 2023;375. https://doi.org/10.1016/j.snb.2022.132953.
[60] Feng C, Shen X, Li B, Liu X, Jing Y, Huang Q, et al. Carbon monoxide impurities in hydrogen detected with resonant photoacoustic cell using a mid-IR laser source. Photoacoustics 2024;36:100585. https://doi.org/10.1016/J.PACS.2024.100585.